Solar wind-magnetosphere coupling during HILDCAAs

S. E. Milan[1*], M. K. Mooney[1] G. Bower[1], A. L. Fleetham[1], S. K. Vines[2], and J. Gjerloev[2]

[1]School of Physics and Astronomy, University of Leicester, Leicester, UK.
[2]Johns Hopkins University Applied Physics Laboratory, USA.

Key Points:

- We study High-Intensity Long-Duration Continuous AE Activity using the expanding/contracting polar cap model
- HILDCAA onsets have typical substorm characteristics, with intense geomagnetic activity in the pre-midnight sector
- High speed solar wind streams produce high but intermittent reconnection rates, driving irregular substorm activity

*Department of Physics and Astronomy, University of Leicester, Leicester LE1 7RH, UK

Corresponding author: Steve Milan, steve.milan@le.ac.uk

Abstract

High-Intensity Long-Duration Continuous AE Activity (HILDCAA) intervals are driven by High Speed solar wind Streams (HSSs) during which the rapidly-varying interplanetary magnetic field (IMF) produces high but intermittent dayside reconnection rates. This results in several days of large, quasi-periodic enhancements in the auroral electrojet (AE) index. There has been debate over whether the enhancements in AE are produced by substorms or whether HILDCAAs represent a distinct class of magnetospheric dynamics. We investigate sixteen HILDCAA events using the expanding/contracting polar cap model as a framework to understand the magnetospheric dynamics occurring during HSSs. Each HILDCAA onset shows variations in open magnetic flux, dayside and nightside reconnection rates, the cross-polar cap potential, and AL that are characteristic of substorms. The enhancements in AE are produced by activity in the pre-midnight sector, which is the typical substorm onset region. The periodicities present in the intermittent IMF determine the exact nature of the activity, producing a range of behaviours from a sequence of isolated substorms, through substorms which run into one-another, to almost continuous geomagnetic activity. The magnitude of magnetic fluctuations, dB/dt, in the pre-midnight sector during HSSs is sufficient to produce a significant risk of Geomagnetically Induced Currents, which can be detrimental to power-grids and pipelines.

Plain Language Summary

High Speed solar wind Streams (HSSs) are several-day periods during which the solar wind is travelling significantly faster than average. It is known that HSSs produce characteristic geomagnetic activity at Earth known as High-Intensity Long-Duration Continuous AE Activity (HILDCAA). The nature of the magnetospheric dynamics occurring in response to HSSs and which produces HILDCAAs is poorly understood. In this study we use a range of magnetic measurements, on the ground and in space, and auroral observations to infer what produces this activity. We show that the activity is caused by a phenomenon known as a magnetospheric substorm, but with characteristics that are somewhat modified as the magnetic field embedded within the solar wind varies in a highly intermittent fashion during HSSs.

1 Introduction

High-Intensity Long-Duration Continuous AE Activity events (HILDCAAs) are intervals when the auroral electrojet indices show high amplitude, quasi-periodic perturbations for several days (Tsurutani & Gonzalez, 1987), as measured by the AE index (Davis & Sugiura, 1966). HILDCAAs are generated during high-speed solar wind streams (HSSs), when the solar wind velocity is of the order of 600 km s^{-1} or greater, the interplanetary magnetic field (IMF) magnitude is just a few nT, but the IMF components undergo Alfvénic fluctuations (i.e., little change in the overall magnitude) with periods of several 10s minutes. These HSSs and their attendant HILDCAAs are often associated with corotating interaction regions (CIRs) and hence maximise in occurrence during the descending phase of the solar cycle (Hajra et al., 2014). The magnetospheric driving and resulting geomagnetic activity during HILDCAAs is in contrast to other solar wind conditions. For instance, during the passage of interplanetary coronal mass ejections (ICMEs) the IMF magnitude can be large and the components vary slowly over many hours or days. ICMEs often result in geomagnetic storms, periods of enhanced ring current (Gonzalez et al., 1994) producing characteristic variations in the Sym-H index (Iyemori, 1990). During more typical solar wind conditions the speed averages 400 km s^{-1}, the IMF magnitude is variable, and the components change stochastically with waiting-times varying between 10s of minutes and hours, to which the magnetosphere responds with substorms. There is debate regarding the exact nature of magnetospheric dynamics which produce HILDCAAs, and whether the quasi-periodic intensifications in AE are the result of substorms,

with Kim et al. (2008) concluding that they are, while Tsurutani et al. (2004) concluded that they are not. In this study we investigate the solar wind-magnetosphere coupling during HILDCAAs, using the expanding/contracting polar cap (ECPC) model as a framework to better understand this mode of solar wind driving.

The ECPC has been used to understand solar wind-magnetosphere-ionosphere coupling (SWMIC) during a range of different solar wind conditions, for instance, explaining the substorm and steady magnetospheric convection (SMC) modes of response to solar wind driving (e.g., Milan et al., 2007, 2008, 2019, 2021; Walach & Milan, 2015). Here we apply the ECPC to HILDCAAs, firstly to gain a better understanding of HILDCAAs, and secondly to investigate SWMIC during a solar wind regime that is quite different from those studied previously with the ECPC. Two key questions are: how does the magnetosphere respond when the variations within the solar wind are shorter than the typical ~ 3 hour substorm repetition rate? and Are AE intensifications during HILDCAAs substorm expansion phases?

The ECPC models the response of the Dungey cycle (Dungey, 1961) to time-varying magnetopause (dayside) and magnetotail (nightside) magnetic reconnection. The dayside rate, Φ_D, depends on conditions in the solar wind, including the solar wind speed, the IMF magnitude, and IMF orientation or clock angle (Milan et al., 2012). The conditions that control the onset and rate of nightside reconnection, Φ_N, are still poorly understood. Φ_D and Φ_N determine the amount of open or polar cap magnetic flux, F_{PC}, in the magnetosphere,

$$\frac{dF_{PC}}{dt} = \Phi_D - \Phi_N, \tag{1}$$

and drive convection within the magnetosphere and ionosphere (Siscoe & Huang, 1985; Cowley & Lockwood, 1992). In turn, the strength of convection, quantified by the cross-polar cap potential or transpolar voltage, Φ_{PC}, where

$$\Phi_{PC} \approx (\Phi_D + \Phi_N)/2 \tag{2}$$

(Lockwood, 1991), controls the magnitude of the auroral electrojets and hence the magnitude of the MI-coupling field-aligned currents or FACs (Milan, 2013). Observations of the size of the polar cap and speed of ionospheric convection can be used to quantify Φ_D and Φ_N (e.g. Hubert et al., 2006; Chisham et al., 2008; Lockwood & McWilliams, 2021). The magnitudes of the eastwards and westwards electrojets are monitored with the AU (auroral upper) and AL (auroral lower) indices, with the AE (auroral electrojet) index being defined as AU − AL (Davis & Sugiura, 1966). The magnitudes of the Hall currents which produce the magnetic perturbations measured by AU and AL are controlled by a combination of the plasma drift speed and the ionospheric conductance in the convection return flow regions, which coincide with the dawn and dusk sectors of the auroral oval. Hence AU and AL are expected to be partially determined by the convection strength measured by Φ_{PC}. The substorm electrojet produces an additional enhancement of AL – the substorm bay – often used as a signature of substorm onset. The PC index measures magnetic perturbations near the pole (Troshichev et al., 2006), which is determined by a combination of drift speed and ionospheric conductance in the central polar cap and hence can be used as a proxy for Φ_{PC} (Milan et al., 2021).

The ECPC explains the substorm cycle (Lockwood & Cowley, 1992), the growth phase being associated with unbalanced dayside reconnection, the expansion phase corresponding to the onset of nightside reconnection, a driven phase with balanced dayside and nightside reconnection, and the recovery phase with unbalanced nightside reconnection (Milan et al., 2003, 2007, 2019, 2021). The left and right columns of Figure 1 summarise the variations of F_{PC} and Φ_{PC} in response to changes in Φ_D and Φ_N, being schematic

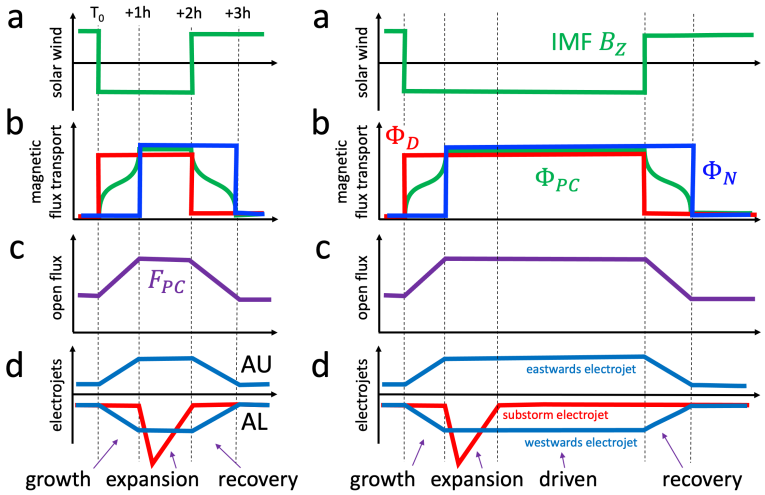

Figure 1. A schematic depiction of the magnetospheric response to changes in the IMF in the context of the expanding/contracting polar cap model (ECPC). (a) A southward turning of the IMF ($B_Z < 0$) followed by a northward turning some time later. (b) The variation of day- and nightside reconnection (Φ_D, red, and Φ_N, blue), and the cross-polar cap potential (Φ_{PC}, green). (c) The variation of the open magnetic flux content of the magnetosphere (F_{PC}). (d) The variation of the AU and AL electrojet indices in response to the eastwards and westwards electrojets (blue curves) and the substorm electrojet (red curve). The AL index is the envelope of the lower red and blue curves. The left column shows the case where the northward turning occurs shortly after the onset of nightside reconnection, such that the magnetosphere undergoes substorm growth, expansion, and recovery phases, each roughly an hour in duration. In the right column the substorm undergoes a driven phase before the eventual northward turning.

representations of the observations presented in columns (d) and (f) of Figure 6 of Milan et al. (2021). On the left, assuming initially that $\Phi_D = \Phi_N = 0$ and the magnetosphere is in a quiescent state, a southward turning of the IMF (panel a) gives $\Phi_D > 0$ (red curve, panel b), $dF_{PC}/dt = \Phi_D$ such that F_{PC} increases (panel c) and excites convection with $\Phi_{PC} \approx \Phi_D/2$ (green curve, panel b): substorm growth phase. Increasing convection leads to enhancements of the AU and AL indices (blue curves, panel d). At some point, typically after an hour-or-so of growth phase, nightside reconnection is triggered, $\Phi_N > 0$ (blue curve, panel b): expansion phase onset. Observations suggest that when this occurs $\Phi_N \approx \Phi_D$, such that $dF_{PC}/dt \approx 0$, $\Phi_{PC} \approx \Phi_D$. The formation of a substorm current wedge (McPherron et al., 1973) and associated substorm electrojet produces the substorm bay in AL (red curve, panel d). Observations show that the bay grows rapidly at first and then decays over approximately an hour. Subsequently, a northward turning of the IMF results in $\Phi_D = 0$ such that $dF_{PC}/dt = -\Phi_N$, the polar cap contracts, with $\Phi_{PC} \approx \Phi_N/2$: substorm recovery phase. At some point nightside reconnection ceases and the magnetosphere returns to a quiescent state.

Figure 1 is essentially a synthesis of Figure 4 of Cowley and Lockwood (1992) and Figure 13 of Kamide and Kokubun (1996), now confirmed by the observations of Milan et al. (2021). In passing we note that we do not agree with the convection patterns presented in Figure 12 of Kamide and Kokubun (1996), but agree with panels (a) and (b) of Figure 3 of Cowley and Lockwood (1992) as representing the convection pattern when dayside and nightside reconnection dominate, respectively.

The right column of Figure 1 shows the same as the left column, except that the IMF remains southwards for a longer period after the onset of the expansion phase. After the substorm bay has subsided the magnetosphere settles down into a prolonged period of balanced dayside and nightside reconnection (DeJong et al., 2008; McWilliams et al., 2008), which Milan et al. (2021) termed the driven phase, and which is synonymous with periods of steady magnetospheric convection or SMC (Sergeev et al., 1996; Walach & Milan, 2015).

In these cases, IMF B_Z changes polarity in a stochastic fashion with a waiting-time distribution with a mode between one and two hours and a long tail extending to many hours (Milan et al., 2021). During HSSs, B_Z varies quasi-periodically with a timescale of several 10s of minutes, often shorter than the typical duration of substorm phases (an hour-or-so each). In this study we investigate how this affects solar wind-magnetosphere coupling during HSSs.

2 Observations

We searched for HILDCAA events in the periods 2000 to 2002 and 2010 to 2017. These intervals coincided with availability of auroral imagery from the IMAGE (Imager for Magnetopause-to-Auroras Global Exploration) mission and measurements of polar field-aligned currents from AMPERE (the Active Magnetosphere and Planetary Electrodynamics Response Experiment), respectively. AMPERE (Anderson et al., 2000; Waters et al., 2001) and IMAGE (Burch, 2000) are used to monitor changes in the size of the polar cap to determine reconnection rates (e.g., Milan et al., 2003, 2007, 2015, 2021; Clausen et al., 2012).

Tsurutani and Gonzalez (1987) defined HILDCAAs as large-amplitude, quasi-periodic variations in AE lasting at least two days, with AE peaking in excess of 1000 nT at some point during the event, and with AE not dipping below 200 nT for more than 2 hours at a time. These are somewhat stringent criteria, and we relaxed them slightly (especially the requirement of short-duration minima in AE) to maximise the number of events we found, as discussed by Prestes et al. (2017). Table 1 lists the events that we consider in this study, with one example from the IMAGE era and 15 from the AMPERE era.

Table 1. The HILDCAA events studied in this paper and the figures they are presented in. Figures S1 to S11 are found in the Supporting Information.

Event	Dates	Figure
1	10 to 14 January 2002	S1
2	29 April to 4 May 2011	S2
3	9 to 17 September 2011	S3
4	3 to 8 June 2012	5
5	29 June to 4 July 2012	S4
6	6 to 11 October 2015	4
7	9 to 12 November 2015	S5
8	9 to 12 December 2015	3
9	30 January to 4 February 2017	S6
10	28 February to 8 March 2017	S7
11	26 March to 1 April 2017	S8
12	21 to 25 April 2017	6
13	17 to 21 August 2017	S9
14	31 August to 5 September 2017	S10
15	14 to 19 September 2017	S11
16	11 to 16 October 2017	S12

The exact nature of each HSS varies from event to event, but all show similar characteristics, including a period of increasing solar wind speed and elevated solar wind density, known as the sheath, followed by the HSS itself. We summarise the characteristics by performing a superposed epoch analysis of our AMPERE examples (events 2 to 16), presented in Figure 2.

The zero epoch is defined as the end of the sheath and the beginning of the HSS, the data are averaged into 6-hour bins, and the time range is from 4 days before to 8 days after the zero epoch. Vertical bars show the standard error on the mean in each bin, which tends to be small. Most parameters, including the solar wind and IMF variables (in Geocentric Solar Magnetic coordinates) and the geomagnetic indices AU, AL (AE = AU − AL), PC, and Sym-H are taken from the OMNI dataset (Papitashvili & King, 2020). $\Phi^{\star}_{D}$, which we use as a proxy for Φ_D, is calculated as

$$\Phi^{\star}_{D} = 3.2 \times 10^{5}\, V_{SW}^{4/3}\, B_{YZ}\, \sin^{9/2}|\theta/2| \tag{3}$$

(Milan et al., 2012), where $B_{YZ} = \left(B_Y^2 + B_Z^2\right)^{1/2}$ and $\theta = \tan^{-1}(B_Y, B_Z)$ is the IMF clock angle. The radius of the region 1 and 2 (R1/R2) current system (Iijima & Potemra, 1976; Milan et al., 2017), Λ, is calculated from AMPERE field-aligned current (FAC) maps (Milan et al., 2015; Milan, 2019). We use Λ as a proxy for F_{PC}. The total FAC magnitude is determined by integrating the absolute FAC values over the polar regions of the northern and southern hemispheres and taking the average (in this way we remove to some degree seasonal variations due to solar-produced conductance).

The solar wind speed (panel a) is 400 km s^{-1} prior to the arrival of the sheath (vertical dashed line) and then rises to exceed 600 km s^{-1} over a period of approximately a day, becoming the HSS-proper (vertical full line). During this rise the density (panel b) increases from 6 cm^{-3} to 11 cm^{-3} and the IMF magnitude (panel c) rises from 6 nT to 11 nT. The enhanced density and IMF magnitude of this sheath is caused by the fast solar wind scooping up slower solar wind travelling ahead of it. The HSS itself lasts two or more days, before a gradual decline to lower speeds again. As will be shown later, al-

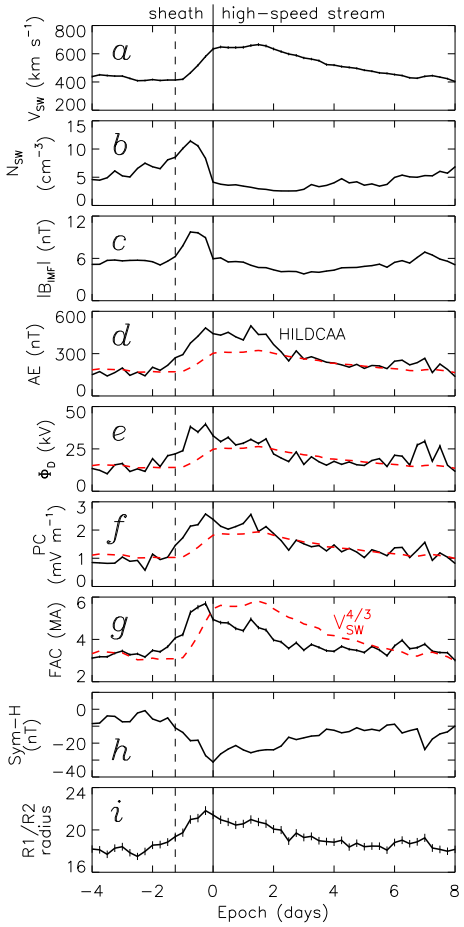

Figure 2. A superposed epoch analysis of 15 High-Speed solar wind Streams (HSSs) and the associated intervals of High-Intensity Long-Duration Continuous AE Activity (HILDCAA). (a) Solar wind speed; (b) solar wind number density; (c) magnitude of the IMF; (d) AE index; (e) dayside reconnection rate; (f) the PC index; (g) the magnitude of the hemispherically-integrated field-aligned currents; (h) the Sym-H index; (i) the radius of the boundary between R1 and R2 FACs, Λ°. In all panels, the standard error on the mean in each bin is shown as vertical bars; in most cases these are too small to be clearly seen. The vertical dashed line shows the approximate onset of the sheath. The vertical solid line shows the zero epoch: the end of the sheath and the beginning of the HSS-proper.

though the IMF magnitude tends to be constant during the HSS, the components undergo short-duration quasi-periodic variations. The Sym-H index (panel h) becomes enhanced (more negative) during the sheath but during the HSS is typically weaker than -50 nT, being approximately -20 nT on average. The AE index (panel d) rises from 200 to 500 nT during the sheath, plateaus for the first two days of the HSS, before declining gradually: the period of enhanced AE is the HILDCAA. Note that the 6-h averaging window in this analysis smoothes over the quasi-periodic fluctuations in AE which are characteristic of HILDCAAs: when not averaged AE peaks at values close to 1000 nT. Other aspects of the behaviour will be discussed later.

We now consider individual Events, shown in Figures 3 to 6; the other Events are shown in the Supplementary Information. Each figure is divided into two groups of pan-

els. The upper panels show the full duration of each event. The panels show: (a) the solar wind speed (green) and density (purple), (b) the B_Y (blue) and B_Z (red) components of the IMF, along with the magnitude of the IMF (grey), (c) the AE index, and (d) the Sym-H index. We also focus on a shorter window within each event, delineated by vertical red bars, with a zoom-in shown in the lower panels. Panel (e) shows the radius of the R1/R2 FAC boundary, Λ, in the northern (orange) and southern (blue) hemispheres, and the average of the two (black) displaced by 5° for clarity. We use Λ as a proxy for F_{PC}. Panel (f) shows the integrated FAC magnitude. Panel (g) shows the PC index (black) and Φ_D (red). Panel (g) shows the AU and AL electrojet indices. Vertical green bars identified by letters are times of note discussed below. Upper case letters (A, B, etc) indicate onsets (see below) whereas lower case letters (a, b, etc.) are discussion points.

The first HILDCAA we discuss, Event 8, is presented in Figure 3. In this event we focus on a time interval that spans pre-sheath, sheath, and early HSS observations, so that we can contrast the behaviour in these three different solar wind regimes.

Events A and B, preceding the sheath, were typical substorms, with B being a particularly clear example. Each event was associated with a southward-turning of the IMF leading to a one-to-two hour period of elevated Φ_D, and each followed the variations in F_{PC} (Λ), Φ_{PC} (PC), and AU/AL as described in the Introduction and sketched in Figure 1. In both cases, the IMF turned northwards approximately 30 minutes after expansion phase onset, such that the full duration of each event was approximately 3 hours. Had the IMF remained southwards for a prolonged period after onset, the magnetosphere would have segued into the driven phase until the eventual subsequent northward-turning.

During the sheath, which encompasses events C, D, and E, the IMF magnitude was somewhat elevated and the fluctuations in B_Y and B_Z increased in tempo. The N-S fluctuations occurred more rapidly than the 3-hour life-cycle of a typical substorm. Despite this, distinct substorm signatures occurred, events C to E, but they ran into each other: northward-turnings of the IMF lead to substorm recovery phase, but southward-turnings occurred before the recovery phase was complete. This even lead to a mini-substorm signature – increase-and-decrease in Λ and weak substorm bay – in between events C and D. There were multiple N-S turnings during the growth phase of event E, such that Λ increased in a step-wise fashion. However, the onset (substorm bay) of event E did not occur until Λ reached a similar level to the previous substorms. This indicates that open flux accumulates in the magnetosphere with each burst of dayside reconnection, but conditions for substorm onset do not occur in the magnetotail until some threshold is reached. We note that for events A to D the IMF turned northwards approximately 30 mins after onset, whereas in event E it remained southwards for longer, such that the duration of the substorm bay was prolonged, that is, event E was approaching a driven-phase substorm.

Into the HSS itself, the IMF components fluctuated even more rapidly. Again, distinct cycles of growth, expansion, and recovery were observed in Λ, with a repetition rate close to 3 hours. The growth phases were intermittent accumulations of open flux, with substorm onset occurring when some F_{PC} threshold was met. Very clearly, Φ_{PC} increased at the onset of each event, indicating the contribution of nightside reconnection to convection. We contrast the variation in Λ in events A and B – clean, sawtooth-like signatures – with the more staggered, step-like changes of events F to I. Steps occurred during both growth and recovery phases as bursts of dayside reconnection came at random intervals throughout each substorm. Similarly, although AU and AL displayed distinct substorm signatures, they had random perturbations superimposed, driven by stochastic changes in dayside driving.

We now turn to other HILDCAAs that illustrate other aspects of the coupling. Figure 4, Event 6, shows a HSS in which there were rapid 10s-minutes fluctuations in B_Z superimposed on a several-hour periodicity. B_Z was predominantly negative (significant

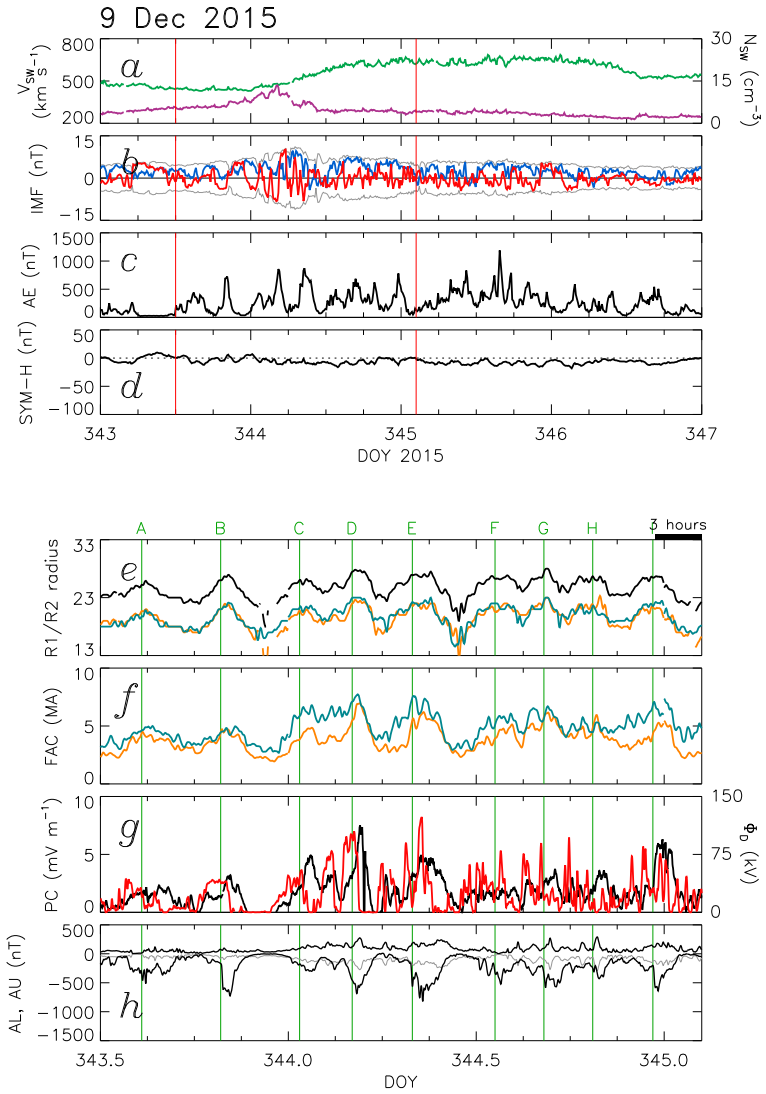

Figure 3. Solar wind and magnetospheric parameters during Event 8. (a) Solar wind speed (green) and number density (purple); (b) the B_Y (blue) and B_Z (red) components of the IMF, and the IMF magnitude (grey); (c) the AE index; (d) the Sym-H index. Vertical red lines delineate the period shown in the lower panels. (e) The radius of the boundary between the R1 and R2 FACs, $\Lambda°$, in the northern (northern) and southern (blue) hemispheres, quantified from observations of the FACs by AMPERE; the average is shown in black, offset by $+5°$ for clarity. (f) The northern (orange) and southern (blue) hemispherically-integrated FACs; (g) The PC index (black) and $\Phi_D^\star$ (red); (h) the AU and AL indices.

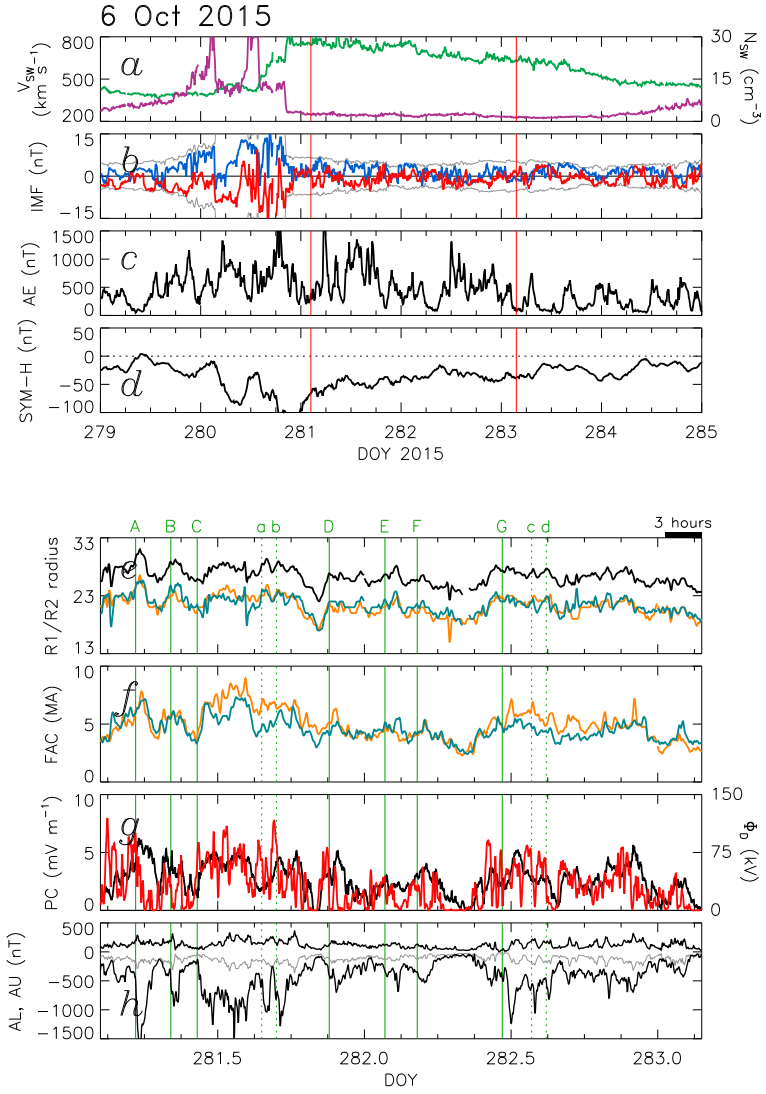

Figure 4. Event 6, presented in the same format as Figure 3.

Φ_D) for long periods, for instance between times C and D and after G, and predominantly positive at other times, before C and between D and G, but with short duration fluctuations superimposed. The first two events, A and B, showed typical substorm characteristics, with a repetition rate of approximately 3 hours driven by two hour-long southward-turnings of the IMF. After C the IMF remained southwards for 9 hours, though with rapid fluctuations superimposed. Following onset at time C, continued dayside reconnection maintained the magnetosphere in a driven phase, with Λ elevated throughout, in which $\Phi_N \approx \Phi_D$. There were, however, small-scale variations in Λ (a and b) associated with bursts in Φ_D, and with bays in AL. This suggests that during on-going driven phases, $\sim$ 1-hour variations in Φ_D can modulate Φ_N; these are similar to the driven-phase onsets discussed by Milan et al. (2021), but on a shorter timescale. Events D, E, and F occurred during a quieter period and were more-typical substorms. Event G was then more similar to the driven phase of event C, again with variations imposed by bursts in Φ_D (c and d).

Figure 5 shows Event 4. In this event, high-frequency fluctuations (minutes) in B_Z were superimposed on longer variations (several hours). The magnetosphere responded

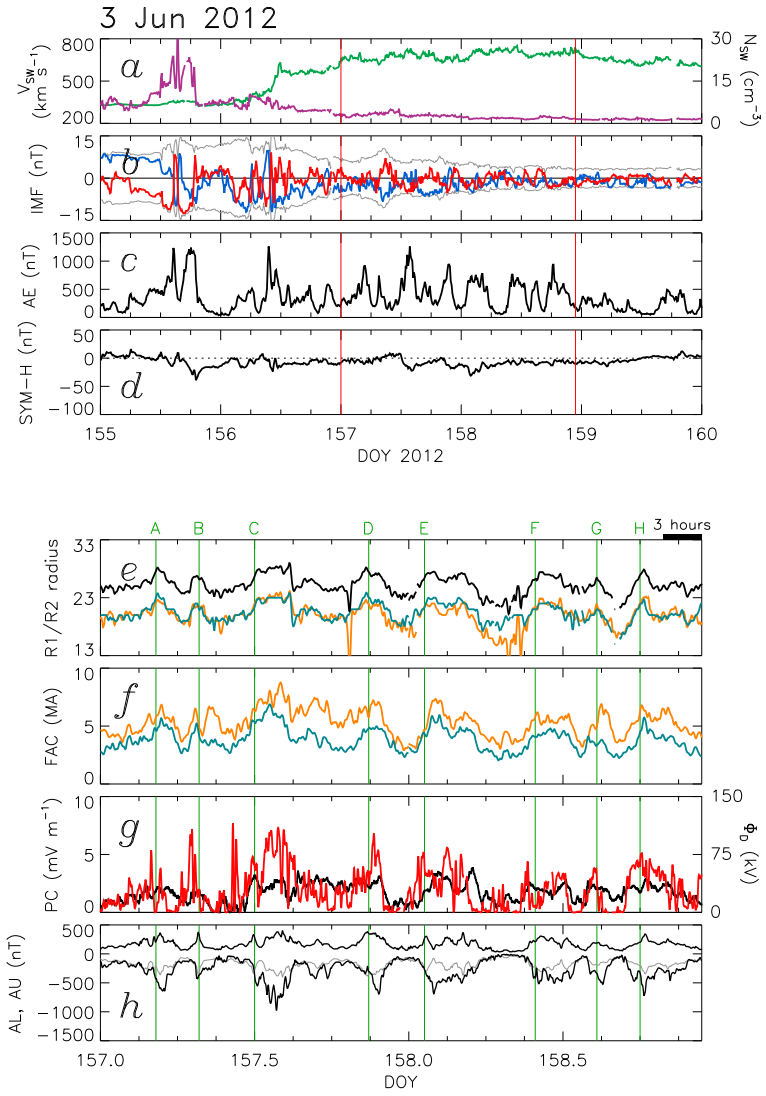

Figure 5. Event 4, presented in the same format as Figure 3.

to each long duration period of $B_Z < 0$ with a substorm-like growth, expansion, and recovery phase. Due to the long periods of $\Phi_D > 0$ many of these substorms had a driven phase (e.g., events C, E, F, H). In contrast, during Event 12, Figure 6, the main quasi-period of fluctuations was close to 1-2 hours. Substorms ran into one-another, and more continuous activity ensued. However, there were still expansions and contractions of the polar cap and identifiable onsets, with a quasi-periodicity close to 3 hours. Figures showing the other events can be found in the Supporting Information. In each case, the response of the magnetosphere to the solar wind driving differed depending on the spectrum of periodicities in the fluctuations of B_Z, especially whether the main periodicities were longer or shorter than the canonical substorm duration. However, in all cases, a quasi-periodic response of 2 to 3 hours can be discerned.

So far we have been using Λ as a proxy for F_{PC} rather than measurements of F_{PC} itself. Figure S1 shows Event 1 which occurred during the IMAGE era, allowing us to use global auroral imagery to estimate F_{PC} (see panel e), determined from identifications of the poleward boundary of the auroral oval provided by Chisham et al. (2022). The data are not continuous due to the orbit of the IMAGE spacecraft, with several-hour

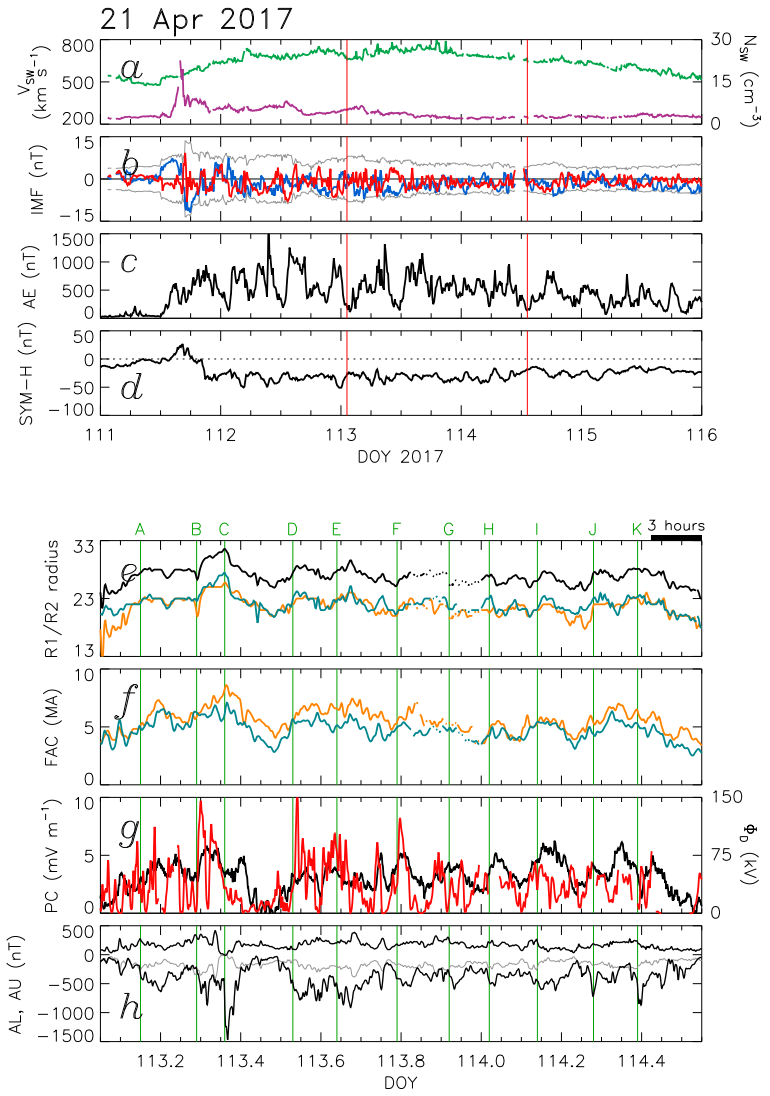

Figure 6. Event 12, presented in the same format as Figure 3.

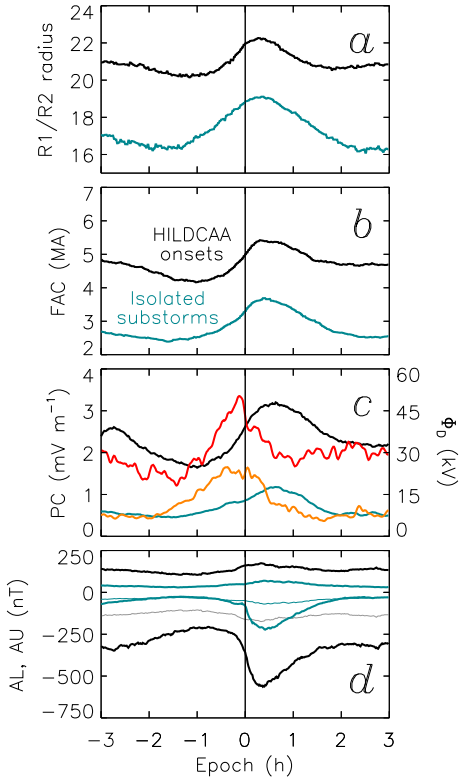

Figure 7. A superposed epoch analysis of individual HILDCAA onsets (black) and isolated substorm onsets (blue). (a) The R1/R2 FAC radius, $\Lambda°$); (b) the hemispherically-integrated FAC magnitude; (c) the PC index and $\Phi_D^\star$ (red/orange); (d) the AU and AL indices.

data gaps every 14 hours. However, this event confirms that HILDCAA onsets are associated with increases and decreases in F_{PC}, where these changes are of the order of 0.2 to 0.3 GWb.

Figure 7 presents a superposed epoch analysis of the individual HILDCAA onsets identified in Events 2 to 16 (except onsets A to E of Event 8 (Figure 3) as these do not occur during the HSS), totalling 129 events. Panels (a) to (d) show Λ, the FAC intensity, the PC index (black) and Φ_D (red) and AU and AL, from 3 hours before to 3 hours after onset. These are compared with a superposed epoch analysis of 101 isolated substorms from 2010 (shown in blue and orange), identified by Milan et al. (2021). Both HILDCAA onsets and substorm onsets show the same general patterns: an increase and decrease in F_{PC} during the growth and recovery phases, similar changes in the strength of the FACs, and a substorm bay in AL beginning at onset. These are driven by an increase in Φ_D leading to the growth phase, during which Φ_{PC} increases, a maximum in Φ_{PC} in the expansion phase, and a reduction during the recovery phase. Φ_D reduces some time after onset as the IMF turns northwards. However, there are distinct differences between HILDCAA and non-HILDCAA onsets: HILDCAA onsets occur on an expanded oval with larger Λ (higher F_{PC}), are associated with stronger FACs and greater electrojet activity. These differences are driven by a significantly higher Φ_D during HILDCAAs. More subtle variations can also be seen. Considering F_{PC}, non-HILDCAA substorms tend to last just over 3 hours from the beginning of the growth phase to the end of the recovery phase, with the growth phase lasting approximately 80 mins. The HILDCAA growth phase is shorter, starting approximately 40 mins before onset, presumably associated with the greater Φ_D. In non-HILDCAA substorms, Φ_D remains, on average,

elevated for 20 mins after onset. However, HILDCAA events have a distinct drop in Φ_D at the time of onset. This could in part be associated with the rapid variations in B_Z seen during HILDCAAs, but may also indicate that northward turnings can trigger onsets. The variation in PC for the HILDCAA onsets shows a secondary peak at -160 mins, emphasising the approximate 3 hour quasi-periodicity of the HILDCAA events. Moreover, during HILDCAAs, $|\mathrm{AL}| >$ AU throughout the period, emphasising that there is near continuous nightside activity. Finally, we note that the variation in integrated FACs mirrors closely the variation in the PC index (Φ_{PC}) and the AU index: this is to be expected as the ionospheric currents which produce the PC and AU magnetic deflections are fed by the FACs.

3 Discussion

We have applied the expanding/contracting polar cap model to HILDCAA events. There has been debate over the nature of the AE enhancements and whether they are produced by substorm expansion phases and attendant formation of a substorm current wedge. Tsurutani et al. (2004) concluded that they were not substorms, and suggested instead that intensifications of the westwards electrojet by prompt penetration of interplanetary electric fields could be the cause. Rout et al. (2022) also concluded that HILDCAAs were not directly related to substorms but produced by the excitation of a global perturbation with a "quasi-resonant frequency" of order 1.5 to 2 hours. On the other hand, Kim et al. (2008) found that energetic particle injections at geosynchronous orbit during HILDCAAs were well-aligned with substorm onsets seen in global auroral imagery, so deduced that most of these activations were indeed substorms. In this study, we find that the variations in AU and AL (and hence AE), F_{PC}, and Φ_{PC}, conform to what is expected due to variations of dayside and nightside reconnection during substorms (Cowley & Lockwood, 1992; Lockwood, 1991; Lockwood & Cowley, 1992; Milan et al., 2021). The picture is somewhat complicated by the highly intermittent nature of Φ_D, due to the Alfvénic fluctuations in the IMF, but the physics is essentially the same: accumulation of open flux by dayside reconnection expands the polar cap and inflates the magnetotail, the growth phase, until conditions are met such that reconnection is triggered in the magnetotail to reclose flux. The onset of tail reconnection, the expansion phase, is accompanied by a bay in AL consistent with the formation of a substorm current wedge (McPherron et al., 1973), and this is the cause of the intensification in AE. Thereafter, if dayside reconnection continues the magnetosphere enters a state of balanced dayside and nightside reconnection, what has been termed the driven phase (Milan et al., 2021). This ends when the IMF turns northwards, dayside reconnection ceases, on-going nightside reconnection causes the polar cap to contract and the tail to deflate: the recovery phase. Nightside reconnection ceases once sufficient flux has been closed. The duration of the driven phase can vary from minutes to several hours (e.g., compare onsets A and C of Event 6 in Figure 4), depending on the variability within the IMF.

The IMF within the HSSs undergoes Alfvénic fluctuations on a variety of timescales ranging from minutes to hours (e.g., Rout et al., 2022). The superposition of long and short timescales results in variability within Φ_D which differs for each HILDCAA event. This in turn controls the magnetospheric response. The typical substorm duration is of the order of 3 hours, in which the growth, expansion, and recovery phases each last approximately one hour (Milan et al., 2021). In some HILDCAA cases, enhancements in Φ_D occur every few (greater than 3) hours and last for several hours each time, for instance in Event 4, Figure 5. In such cases, the repetition timescale is somewhat longer than the typical substorm cycle, and a sequence of essentially isolated substorms results, some with prolonged driven phases. Short timescale variability superimposed on this long term behaviour gives the substorms a somewhat "ragged" appearance (cf. the "smoother" appearance of onsets A and B of Event 8, Figure 3, which are not HILDCAA onsets). In some cases the variability in Φ_D occurs on timescales shorter than 3 hours, e.g., Event

12, Figure 6. Now more continuous activity ensues, with few periods of quiescence. It is difficult to identify individual onsets with any certainty, though there are still expansions and contractions of the polar cap and enhancements in AL, reminiscent of substorms. This variability occurs with a quasi-periodicity close to 2 to 3 hours, and we suggest that this is controlled by the expanding/contracting timescale associated with reconnection at the magnetopause and in the magnetotail. There are other cases, e.g. Events 5 and 9, Figures S3 and S5, in which the main variability in Φ_D has a periodicity close to 3 hours and the substorms begin to run into each other, a new growth phase beginning even before the previous recovery phase is complete. In Event 6, Figure 4, the variability is such that there are several-hour periods of $B_Z > 0$ and several-hour periods of $B_Z < 0$, with shorter duration variability superimposed on top. This leads to periods of continuous activity interspersed with periods of lower activity or quiescence.

As well as being intermittent, Φ_D tends to be larger than average during HSSs. Equation 3 shows that Φ_D is high when the solar wind speed is high, the magnitude of the IMF is high, and when the IMF is directed southwards. During HSSs the IMF magnitude is about the solar wind average and uniform, but Alfvénic fluctuations cause changes in the clock angle giving the intermittency. On the other hand, V_{SW} is high and this produces the enhancement in Φ_D. We return to the superposed epoch analysis of Figure 2, specifically panels (d) to (g). In each of these panels, $V_{SW}^{4/3}$ is superimposed (red dashed line), scaled to be similar to each parameter at the start and end of the interval. Unsurprisingly, Φ_D (panel e) matches $V_{SW}^{4/3}$ well prior to the sheath arrival and during the HSS and its decline. However, Φ_D exceeds $V_{SW}^{4/3}$ during the sheath passage, showing that the enhanced IMF magnitude in the sheath is driving the higher coupling rate at this time. We expect from Equation 2 that averaged over the substorm cycle $\langle\Phi_N\rangle = \langle\Phi_D\rangle = \langle\Phi_{PC}\rangle$ and, indeed, the variation of PC, our proxy for Φ_{PC}, shows a similar behaviour to Φ_D. Interestingly, AE (panel d) and the magnitude of the FACs (panel g) do not follow the same behaviour. Both the AE and FAC magnitude are elevated during the sheath, as expected, but AE is underestimated and FAC magnitude overestimated by $V_{SW}^{4/3}$ during the HSS. Clearly, these current systems, mainly the substorm current wedge and R1/R2 system, respectively, are not solely controlled by Φ_D, and other factors, presumably including ionospheric conductivity, play an important role. Finally, panel (i) shows the variation in F_{PC}, being elevated during the sheath, and somewhat elevated during the HSS (consistent with panel (a) of Figure 7). An anticorrelation between F_{PC} and Sym-H has previously been reported (e.g., Schulz, 1997; Milan, Hutchinson, et al., 2009; Milan et al., 2021) and that is consistent with the behaviour seen in panels (h) and (i).

HILDCAA onsets differ from typical substorms due to the high values of Φ_D. The three-hour duration of an isolated substorm is driven by the characteristic loading and unloading timescales of the magnetosphere. Milan et al. (2021) showed that for a typical substorm, the growth phase lasts approximately 80 minutes, with an average Φ_D of 25 kV. During HILDCAAs, Φ_D peaks at values much greater than this, 75 kV, due to the strong dependence of Φ_D on V_{SW}. This results in shorter growth phases for HILDCAA events (Figure 8a). Many HILDCAA events are also shorter than typical substorms as northward turnings are frequent, reducing the duration of the expansion or driven phases of the events (though this depends on the details of the variability within B_Z). If the fluctuations occur more rapidly that the substorm timescale, then substorms can merge into one-another, resembling a driven phase, but with Φ_D-driven intensifications. Even more rapid fluctuations result in the magnetosphere integrating over the intermittent accumulations of open flux, seeming to return to a 2-to-3-hour quasi-periodicity, though with onsets being rather indistinct.

The intermittent Φ_D during HILDCAA growth phases leads to F_{PC} increasing in steps until onset occurs. That HILDCAA growth phases tend to be shorter than typical substorm growth phases, due to Φ_D being large, suggests that onset is caused by some threshold in F_{PC} being reached. This threshold, in turn, depends on Sym-H and/or some

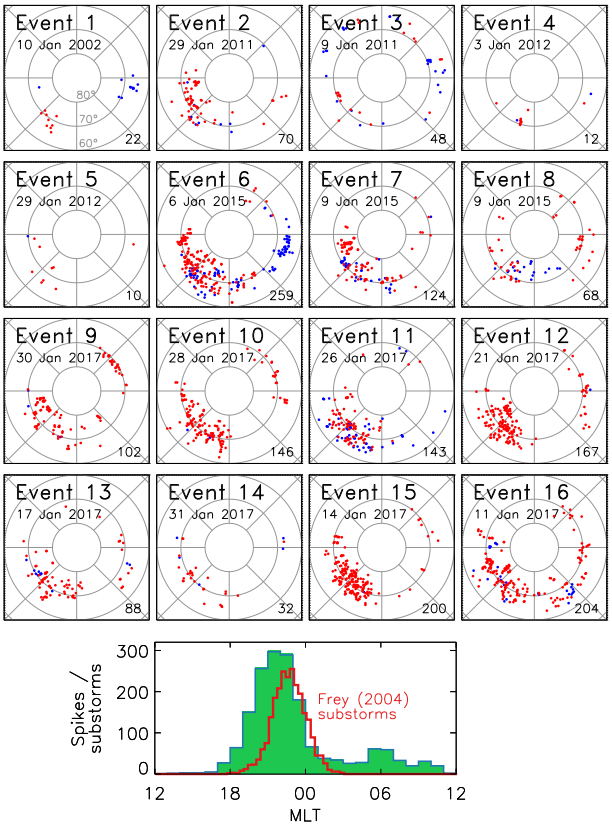

Figure 8. The occurrence of $|dB/dt| > 300$ nT min^{-1} during each event, presented on a magnetic latitude and local time coordinate system, with noon towards the top and dawn to the right. Circles indicate geomagnetic latitudes in steps of 10°. Blue and red dots indicate "spikes" occurring during the sheath and the HSS of each event, respectively. Numbers in the bottom right of each panel show the number of spikes in each event. The lower panel shows the MLT distribution of spikes for all 16 events. Superimposed is the substorm-onset distribution reported by Frey et al. (2004).

other factor, as it does for typical substorms (Milan, Hutchinson, et al., 2009; Milan et al., 2021) . The level of F_{PC} at onset in turn controls the intensity of the resulting substorm, including the magnitude of the AL bay (Milan, Grocott, et al., 2009). That HILDCAAs occur with an elevated F_{PC} explains in part why the AE excursions are so large during HSSs.

We have suggested that HILDCAA onsets are most likely substorm onsets occurring in response to intermittent Φ_D during HSSs. We now test this by determining the local time at which the "spike" in AE or bay in AL is generated, information that is not provided by the indices themselves. We use data from the SuperMAG database of ground-based magnetometers (Gjerloev, 2012) to determine where sudden changes in the magnetic field occur during our 16 Events, that is occurrences of "large dB/dt" or magnetic "spikes". We calculate dB/dt by finding the difference between successive 1-min measurements of the magnetic field at each SuperMAG station, in each of the north-south, east-west, and up-down components (see, e.g., Schillings et al., 2022; Milan et al., 2023, for more detail on the methodology). We identify times of $|dB/dt| > 300$ nT min^{-1} as significant spikes which likely correspond to jumps in the AE or AL indices, and which can also produce Geomagnetically Induced Currents (GICs) which can be detrimental

to ground-based technological systems. Several studies (e.g., Schillings et al., 2022) have shown hotspots of spikes in the pre-midnight and dawn sectors during periods of geomagnetic disturbance. The pre-midnight spikes are identified as being associated with energetic substorms. Figure 8 shows the locations of large spikes during each of our events in a magnetic latitude and magnetic local time coordinate system, in blue or red if they occur during the sheath or the HSS, respectively. The majority of HSS events occur in the pre-midnight sector, with few at dawn. The lower panel shows the local time distribution of spikes from all events, in bins of 1-h of MLT.

If HILDCAA onsets were produced by intensifications of the westwards electrojet by prompt penetration of interplanetary electric fields, as suggested by Tsurutani et al. (2004), the spikes would be expected to be located at dawn, not pre-midnight as seen. For reference, we superimpose the local time distribution (in 20-min bins) of auroral substorm onsets found by Frey et al. (2004) for the first 2.5 years of the IMAGE mission. Our pre-midnight spike distribution matches this well, consistent with the observations of Kim et al. (2008), but extends 1-2 h of MLT to the west; we interpret this as magnetic perturbations produced by the westward-travelling surge (WTS), which typically propagates westwards following substorm onset. We conclude that the AE/AL disturbances during HILDCAAs are rather associated with substorms, and that these disturbances are sufficiently intense to produce hazardous GICs. We note that some events also display a population of spikes near 09 MLT (e.g., Events 9 and 10), which have been attributed to large dB/dt associated with ULF waves generated during periods of high solar wind speed (e.g., Milan et al., 2023), and so might be expected during HSSs.

4 Conclusions

The geomagnetic activity occurring during intervals of High-Intensity Long-Duration Continuous AE Activity (HILDCAAs) is characteristic of substorms. These substorms are of high intensity due to the high but intermittent dayside reconnection rate produced by fast solar wind and quasi-periodically varying IMF during High Speed solar wind Streams (HSSs). Magnetospheric open flux, dayside and nightside reconnection rates, cross-polar cap potential, and the AL index all show variations which are consistent with those expected for substorms in the expanding/contracting polar cap model, though are more intense than typical substorms due to elevated solar wind driving. Moreover, the enhancements in AE are produced by activity confined to the pre-midnight sector, consistent with the substorm onset region, and somewhat to the west of this, possibly associated with the westward-travelling surge. The level of dB/dt during the HILDCAA onsets is sufficient to produce hazardous Geomagnetically Induced Currents (GICs).

The exact nature of the response of the magnetosphere to each HSS differs, depending on the periodicities present in the IMF. If the periodicity is longer than the typical substorm duration (approximately three hours) then a sequence of isolated substorms ensues. If the periodicity is close to the substorm duration then substorms run into one-another. If the periodicity is even shorter then almost continuous auroral activity results.

5 Open Research

Advanced Magnetosphere and Planetary Electrodynamics Response Experiment (AMPERE) data were obtained from JHU/APL (`http://ampere.jhuapl.edu/dataget/index.html`) and processed using software provided (`http://ampere.jhuapl.edu/`). The AMPERE FAC radii dataset (Milan, 2019) is available at `https://doi.org/10.25392/leicester.data.11294861.v1`. The high resolution (1-min) OMNI data were obtained from the NASA Goddard Space Flight Center (GSFC) Space Physics Data Facility OMNIWeb portal at `https://omniweb.gsfc.nasa.gov/form/om_filt_min.html`). The 1-min cadence ("low fidelity") SuperMAG data were obtained from NASA GSFC through the SuperMAG portal at `https://supermag.jhuapl.edu/mag/?fidelity=low`.

Acknowledgments

SEM and MKM were supported by the Science and Technology Facilities Council (STFC), UK, grant no. ST/W00089X/1. Both SEM and GEB were supported by the Natural Environment Research Council (NERC), UK, grant no. NE/W006766/1. ALF was supported by an STFC studentship. We acknowledge use of NASA/GSFC's Space Physics Data Facility's CDAWeb service (at `http://cdaweb.gsfc.nasa.gov`), and OMNI data.

For the SuperMAG ground magnetometer data we gratefully acknowledge: INTERMAGNET, Alan Thomson; CARISMA, PI Ian Mann; CANMOS, Geomagnetism Unit of the Geological Survey of Canada; The S-RAMP Database, PI K. Yumoto and Dr. K. Shiokawa; The SPIDR database; AARI, PI Oleg Troshichev; The MACCS program, PI M. Engebretson; GIMA; MEASURE, UCLA IGPP and Florida Institute of Technology; SAMBA, PI Eftyhia Zesta; 210 Chain, PI K. Yumoto; SAMNET, PI Farideh Honary; IMAGE, PI Liisa Juusola; Finnish Meteorological Institute, PI Liisa Juusola; Sodankylä Geophysical Observatory, PI Tero Raita; UiT the Arctic University of Norway, Tromsø Geophysical Observatory, PI Magnar G. Johnsen; GFZ German Research Centre For Geosciences, PI Jürgen Matzka; Institute of Geophysics, Polish Academy of Sciences, PI Anne Neska and Jan Reda; Polar Geophysical Institute, PI Alexander Yahnin and Yarolav Sakharov; Geological Survey of Sweden, PI Gerhard Schwarz; Swedish Institute of Space Physics, PI Masatoshi Yamauchi; AUTUMN, PI Martin Connors; DTU Space, Thom Edwards and PI Anna Willer; South Pole and McMurdo Magnetometer, PI's Louis J. Lanzarotti and Alan T. Weatherwax; ICESTAR; RAPIDMAG; British Artarctic Survey; McMac, PI Dr. Peter Chi; BGS, PI Dr. Susan Macmillan; Pushkov Institute of Terrestrial Magnetism, Ionosphere and Radio Wave Propagation (IZMIRAN); MFGI, PI B. Heilig; Institute of Geophysics, Polish Academy of Sciences, PI Anne Neska and Jan Reda; University of L'Aquila, PI M. Vellante; BCMT, V. Lesur and A. Chambodut; Data obtained in cooperation with Geoscience Australia, PI Andrew Lewis; AALPIP, co-PIs Bob Clauer and Michael Hartinger; MagStar, PI Jennifer Gannon; SuperMAG, PI Jesper W. Gjerloev; Data obtained in cooperation with the Australian Bureau of Meteorology, PI Richard Marshall.

References

Anderson, B., Takahashi, K., & Toth, B. (2000). Sensing global Birkeland currents with Iridium® engineering magnetometer data. *Geophysical Research Letters*, *27*(24), 4045–4048. doi: https://doi.org/10.1029/2000GL000094

Burch, J. (2000). IMAGE mission overview. *Space Science Reviews*, *91*(1-2), 1–14. doi: https://doi.org/10.1023/A:1005245323115

Chisham, G., Burrell, A., Thomas, E., & Chen, Y.-J. (2022). Ionospheric boundaries derived from auroral images. *Journal of Geophysical Research: Space Physics*, *127*(7), e2022JA030622. doi: https://doi.org/10.1029/2022JA030622

Chisham, G., Freeman, M., Abel, G., Lam, M., Pinnock, M., Coleman, I., ... Villain, J.-P. (2008). Remote sensing of the spatial and temporal structure of magnetopause and magnetotail reconnection from the ionosphere. *Reviews of Geophysics*, *46*(1). doi: https://doi.org/10.1029/2007RG000223

Clausen, L., Baker, J., Ruohoniemi, J., Milan, S., & Anderson, B. (2012). Dynamics of the region 1 Birkeland current oval derived from the Active Magnetosphere and Planetary Electrodynamics Response Experiment (AMPERE). *Journal of Geophysical Research: Space Physics*, *117*(A6). doi: https://doi.org/10.1029/2012JA017666

Cowley, S., & Lockwood, M. (1992). Excitation and decay of solar wind-driven flows in the magnetosphere-ionosphere system. *Annales Geophysicae*, *10*, 103–115.

Davis, T. N., & Sugiura, M. (1966). Auroral electrojet activity index AE and its universal time variations. *Journal of Geophysical Research*, *71*(3), 785–801.

DeJong, A., Ridley, A., & Clauer, C. (2008). Balanced reconnection intervals: Four

case studies. *Annales Geophysicae*.

Dungey, J. (1961). Interplanetary magnetic field and the auroral zones. *Physical Review Letters*, *6*(2), 47.

Frey, H., Mende, S., Angelopoulos, V., & Donovan, E. (2004). Substorm onset observations by IMAGE-FUV. *Journal of Geophysical Research: Space Physics*, *109*(A10).

Gjerloev, J. (2012). The SuperMAG data processing technique. *Journal of Geophysical Research: Space Physics*, *117*(A9). doi: https://doi.org/10.1029/2012JA017683

Gonzalez, W., Joselyn, J.-A., Kamide, Y., Kroehl, H., Rostoker, G., Tsurutani, B., & Vasyliunas, V. (1994). What is a geomagnetic storm? *Journal of Geophysical Research: Space Physics*, *99*(A4), 5771–5792. doi: https://doi.org/10.1029/93JA02867

Hajra, R., Echer, E., Tsurutani, B. T., & Gonzalez, W. D. (2014). Superposed epoch analyses of hildcaas and their interplanetary drivers: Solar cycle and seasonal dependences. *Journal of Atmospheric and Solar-Terrestrial Physics*, *121*, 24–31. doi: https://doi.org/10.1016/j.jastp.2014.09.012

Hubert, B., Milan, S., Grocott, A., Blockx, C., Cowley, S., & Gérard, J.-C. (2006). Dayside and nightside reconnection rates inferred from IMAGE FUV and Super Dual Auroral Radar Network data. *Journal of Geophysical Research: Space Physics*, *111*(A3).

Iijima, T., & Potemra, T. (1976). The amplitude distribution of field-aligned currents at northern high latitudes observed by Triad. *Journal of Geophysical Research*, *81*(13), 2165–2174. doi: https://doi.org/10.1029/JA081i013p02165

Iyemori, T. (1990). Storm-time magnetospheric currents inferred from mid-latitude geomagnetic field variations. *Journal of Geomagnetism and Geoelectricity*, *42*(11), 1249–1265.

Kamide, Y., & Kokubun, S. (1996). Two-component auroral electrojet: Importance for substorm studies. *Journal of Geophysical Research: Space Physics*, *101*(A6), 13027–13046.

Kim, H.-J., Lee, D.-Y., & Lyons, L. (2008). Are repetitive particle injections during high-speed solar wind streams classic substorms? *Journal of Geophysical Research: Space Physics*, *113*(A8). doi: https://doi.org/10.1029/2007JA012847

Lockwood, M. (1991). On flow reversal boundaries and transpolar voltage in average models of high-latitude convection. *Planetary and space science*, *39*(3), 397–409.

Lockwood, M., & Cowley, S. (1992). Ionospheric convection and the substorm cycle. *Proceedings of the International Conference on Substorms (ICS-1)*, 99–109.

Lockwood, M., & McWilliams, K. A. (2021). On optimum solar wind–magnetosphere coupling functions for transpolar voltage and planetary geomagnetic activity. *Journal of Geophysical Research: Space Physics*, e2021JA029946. doi: https://doi.org/10.1029/2021JA029946

McPherron, R. L., Russell, C. T., & Aubry, M. P. (1973). Satellite studies of magnetospheric substorms on August 15, 1968: 9. Phenomenological model for substorms. *Journal of Geophysical Research*, *78*(16), 3131–3149. doi: https://doi.org/10.1029/JA078i016p03131

McWilliams, K., Pfeifer, J., & McPherron, R. (2008). Steady magnetospheric convection selection criteria: Implications of global superdarn convection measurements. *Geophysical research letters*, *35*(9).

Milan, S. (2013). Modeling Birkeland currents in the expanding/contracting polar cap paradigm. *Journal of Geophysical Research: Space Physics*, *118*(9), 5532–5542. doi: https://doi.org/10.1002/jgra.50393

Milan, S. (2019). *AMPERE R1/R2 FAC radii. figshare. Dataset.* `https://doi.org/10.25392/leicester.data.11294861.v1`. doi: 10.25392/leicester.data.11294861.v1

Milan, S., Boakes, P., & Hubert, B. (2008). Response of the expanding/contracting polar cap to weak and strong solar wind driving: Implications for substorm onset. *Journal of Geophysical Research: Space Physics*, *113*(A9).

Milan, S., Carter, J., Korth, H., & Anderson, B. (2015). Principal component analysis of Birkeland currents determined by the Active Magnetosphere and Planetary Electrodynamics Response Experiment. *Journal of Geophysical Research: Space Physics*, *120*(12), 10–415. doi: https://doi.org/10.1002/2015JA021680

Milan, S., Carter, J., Sangha, H., Bower, G., & Anderson, B. (2021). Magnetospheric flux throughput in the Dungey cycle: Identification of convection state during 2010. *Journal of Geophysical Research: Space Physics*, *126*(2), e2020JA028437. doi: https://doi.org/10.1029/2020JA028437

Milan, S., Clausen, L., Coxon, J., Carter, J., Walach, M.-T., Laundal, K., ... others (2017). Overview of solar wind–magnetosphere–ionosphere–atmosphere coupling and the generation of magnetospheric currents. *Space Science Reviews*, *206*(1-4), 547–573. doi: https://doi.org/10.1007/s11214-017-0333-0

Milan, S., Gosling, J., & Hubert, B. (2012). Relationship between interplanetary parameters and the magnetopause reconnection rate quantified from observations of the expanding polar cap. *Journal of Geophysical Research: Space Physics*, *117*(A3). doi: https://doi.org/10.1029/2011JA017082

Milan, S., Grocott, A., Forsyth, C., Imber, S., Boakes, P., & Hubert, B. (2009). A superposed epoch analysis of auroral evolution during substorm growth, onset and recovery: Open magnetic flux control of substorm intensity. *Annales Geophysicae*, *27*(2), 659–668.

Milan, S., Hutchinson, J., Boakes, P., & Hubert, B. (2009). Influences on the radius of the auroral oval. *Annales Geophysicae*, *27*(7), 2913–2924. doi: https://doi.org/10.5194/angeo-27-2913-2009

Milan, S., Imber, S., Fleetham, A., & Gjerloev, J. (2023). Solar cycle and solar wind dependence of the occurrence of large db/dt events at high latitudes. *Journal of Geophysical Research: Space Physics*, *128*(4), e2022JA030953. doi: https://doi.org/10.1029/2022JA030953

Milan, S., Lester, M., Cowley, S., Oksavik, K., Brittnacher, M., Greenwald, R., ... Villain, J.-P. (2003). Variations in the polar cap area during two substorm cycles. *Annales Geophysicae*, *21*(5), 1121–1140.

Milan, S., Provan, G., & Hubert, B. (2007). Magnetic flux transport in the Dungey cycle: A survey of dayside and nightside reconnection rates. *Journal of Geophysical Research: Space Physics*, *112*(A1). doi: https://doi.org/10.1029/2006JA011642

Milan, S., Walach, M.-T., Carter, J., Sangha, H., & Anderson, B. (2019). Substorm onset latitude and the steadiness of magnetospheric convection. *Journal of Geophysical Research: Space Physics*, *124*(3), 1738–1752.

Papitashvili, N., & King, J. (2020). *"omni 1-min dat" [data set], NASA Space Physics Data Facility.* doi: https://doi.org/10.48322/45bb-8792

Prestes, A., Klausner, V., González, A., & Serra, S. (2017). Statistical analysis of solar wind parameters and geomagnetic indices during HILDCAA/HILDCAA* occurrences between 1998 and 2007. *Advances in Space Research*, *60*(8), 1850–1865. doi: https://doi.org/10.1016/j.asr.2017.06.023

Rout, D., Singh, R., Pandey, K., Pant, T., Stolle, C., Chakrabarty, D., ... Bag, T. (2022). Evidence for presence of a global quasi-resonant mode of oscillations during high-intensity long-duration continuous AE activity (HILDCAA) events. *Earth, Planets and Space*, *74*(1), 1–11. doi: https://doi.org/10.1186/s40623-022-01642-1

Schillings, A., Palin, L., Opgenoorth, H., Hamrin, M., Rosenqvist, L., Gjerloev, J., ... Barnes, R. (2022). Distribution and occurrence frequency of dB/dt spikes during magnetic storms 1980-2020. *Space Weather*, *20*, e2021SW002953. doi: https://doi.org/10.1029/2021SW002953

637 Schulz, M. (1997). Direct influence of ring current on auroral oval diameter. *Journal*
638 *of Geophysical Research: Space Physics*, *102*(A7), 14149–14154. doi: https://
639 doi.org/10.1029/97JA00827
640 Sergeev, V., Pellinen, R. J., & Pulkkinen, T. (1996). Steady magnetospheric convec-
641 tion: A review of recent results. *Space Science Reviews*, *75*(3-4), 551–604.
642 Siscoe, G., & Huang, T. (1985). Polar cap inflation and deflation. *Journal of Geo-*
643 *physical Research: Space Physics*, *90*(A1), 543–547.
644 Troshichev, O., Janzhura, A., & Stauning, P. (2006). Unified PCN and PCS indices:
645 Method of calculation, physical sense, and dependence on the IMF azimuthal
646 and northward components. *Journal of Geophysical Research: Space Physics*,
647 *111*(A5).
648 Tsurutani, B., & Gonzalez, W. (1987). The cause of high-intensity long-duration
649 continuous AE activity (HILDCAAs): Interplanetary Alfvén wave trains.
650 *Planetary and Space Science*, *35*(4), 405–412. doi: https://doi.org/10.1016/
651 0032-0633(87)90097-3
652 Tsurutani, B., Gonzalez, W., Guarnieri, F., Kamide, Y., Zhou, X., & Arballo, J.
653 (2004). Are high-intensity long-duration continuous AE activity (HILD-
654 CAA) events substorm expansion events? *Journal of Atmospheric and*
655 *Solar-Terrestrial Physics*, *66*(2), 167–176. doi: https://doi.org/10.1016/
656 j.jastp.2003.08.015
657 Walach, M.-T., & Milan, S. (2015). Are steady magnetospheric convection events
658 prolonged substorms? *Journal of Geophysical Research: Space Physics*, *120*(3),
659 1751–1758.
660 Waters, C., Anderson, B., & Liou, K. (2001). Estimation of global field aligned
661 currents using the Iridium® system magnetometer data. *Geophysical Research*
662 *Letters*, *28*(11), 2165–2168. doi: https://doi.org/10.1029/2000GL012725